

Contents lists available at ScienceDirect

Petroleum Science

journal homepage: www.keaipublishing.com/en/journals/petroleum-science



Original Paper

Hybrid absorbing boundary condition based on transmitting boundary and its application in 3D fractional viscoacoustic modeling



Song-Ling Li, Ying Shi*, Ning Wang, Wei-Hong Wang, Xuan Ke

School of Earth Sciences, Northeast Petroleum University, Daging, Heilongjiang 163318, China

ARTICLE INFO

Article history: Received 4 January 2022 Received in revised form 19 June 2022 Accepted 15 September 2022 Available online 20 September 2022

Edited by Jie Hao

Keywords:
Hybrid absorbing boundary
Numerical simulation
Transmitting boundary
Fractional viscoacoustic wave equation

ABSTRACT

An accurate numerical simulation for wave equations is essential for understanding of wave propagation in the earth's interior as well as full waveform inversion and reverse time migration. However, due to computational cost and hardware capability limitations, numerical simulations are often performed within a finite domain. Thus, an adequate absorbing boundary condition (ABC) is indispensable for obtaining accurate numerical simulation results. In this study, we develop a hybrid ABC based on a transmitting boundary, which is referred to as THABC, to eliminate artificial boundary reflections in 3D second-order fractional viscoacoustic numerical simulations. Furthermore, we propose an adaptive weighted coefficient to reconcile the transmitting and viscoacoustic wavefields in THABC. Through several numerical examples, we determine that the proposed THABC approach is characterized by the following benefits. First, with the same number of absorbing layers, THABC exhibits a better ability in eliminating boundary reflection than traditional ABC schemes. Second, THABC is more effective in computation, since it only requires the wavefields at the current and last time steps to solve the transmitting formula within the absorbing layers. Benefiting from a simple but effective combination between the transmitting equation and the second-order wave equation, our scheme performs well in the 3D fractional Laplacian viscoacoustic numerical simulation.

© 2022 The Authors. Publishing services by Elsevier B.V. on behalf of KeAi Communications Co. Ltd. This is an open access article under the CC BY-NC-ND license (http://creativecommons.org/licenses/by-nc-nd/4.0/).

1. Introduction

Numerical simulation is crucial in comprehending seismic wave propagation mechanisms and is a prerequisite for imaging and subsurface structure inversion (Li et al., 2017; Wang et al., 2017, 2019a; Liu et al., 2020; Yao et al., 2020; Zou et al., 2020; Ren et al., 2022). Seismic forward modeling can be implemented using finitedifference (Alford et al., 1974; Virieux, 1984), finite element (Lysmer and Drake, 1972; Khataniar and Peters, 1991), pseudo-spectral (Kreiss and Oliger, 1972; Fornberg, 2012), one-step method (Zhang and Zhang, 2009; Liu and Zhang, 2019), and several other methods. Because of computational cost and hardware capability limitations, numerical simulations are often performed within a finite domain, although the subsurface can be considered a semiinfinite medium. If these artificial boundary reflections are not appropriately processed, erroneous events might appear in seismic imaging and inversion (Zhang and Shi, 2019). Therefore, these nonphysical boundary reflections must be eliminated to perform accurate seismic simulations, imaging, and inversion (Roger et al.,

2014; Ren et al., 2017; Wang et al., 2019b; Ren et al., 2021; Wang et al., 2021; Zhang et al., 2021).

Early attempts to achieve nonreflecting absorbing boundary conditions (ABCs) are divided into three categories. The first one is based on wavefield energy attenuation, where the damping layers are introduced to absorb boundary reflections (Cerjan et al., 1985; Berenger, 1994; Collino and Tsogka, 2001; Yao et al., 2018). Among them, PML is the most extensively used scheme and is one of the most effective and stable ABCs (Chew and Weedon, 1994). However, conventional PML requires splitting each variable, making them either perpendicular or parallel to the boundary, and the wave equation must be modified according to attenuation factors. Kuzuoglu and Mittra (1996) proposed a general complex frequency shifted (CFS) method to absorb the evanescent waves more effectively. To effectively implement the CFS-PML method, Roden and Gedney (2000) proposed a convolution PML (CPML) scheme to avoid wavefield splitting in numerical simulations. However, most PML or CPML methods are more suitable for first-order velocitystress equations but complicated for second-order equations (Komatitsch and Tromp, 2003; Zhuang et al., 2020). CPML usually needs to introduce auxiliary variables or equations when applied to the second-order equation, leading to additional computation

^{*} Corresponding author.

E-mail address: shiying@nepu.edu.cn (Y. Shi).

burdens and storage (Martin et al., 2010; Zhang and Shen, 2010; Li and Matar, 2010; Duru and Kreiss, 2012; Ma et al., 2019). Thus, this absorbing boundary might degrade the computational efficiency in seismic imaging and inversion, especially for large-scale 3D problems (Zhang et al., 2020).

The second scheme is based on one-way wave equation (Clayton and Engquist, 1977; Higdon, 1986, 1987, 1991; Heidari and Guddati, 2006), which merely requires one boundary layer to suppress boundary reflections. Even though the low-order one-way wave equations perform well in computational efficiency, memory costs, and mathematical form, the incident angle limits the absorbing effect. High-order one-way wave equations can reduce the incident angle limitation (Rabinovich et al., 2010; Song et al., 2015); however, this scheme is not frequently selected due to its complex mathematical form or zero-frequency drift instability. Alternatively, the transmitting boundary is universal and easy to implement (Liao et al., 2002). However, because solving the two-way and one-way wave equations are different in conventional one-way wave boundary conditions, all the above schemes introduce boundary reflections arising from the sudden transformation between the internal physical domain and boundary.

The third scheme is the hybrid ABC (HABC). Liu and Sen (2010) first introduced transition regions to remove mutations between different equations, in which a linearly weighted coefficient is used to glue the Clayton one-way and two-way wavefields. Two factors affect the absorbing effect of HABC. The first is the choice of a one-way wave equation. Liu and Sen (2012) used the Higdon one-way wave equation to constitute the HABC (HHABC) and applied it in second-order elastic wavefield simulations. Ren and Liu (2014) extended the HHABC to a first-order elastic wave equation and validated its superiority in absorbing effect and computational ef-

next time step as an initial condition in the boundary, whereas THABC only requires wavefields at the current and last time steps. Thus, THABC has a high potential to improve the computational efficiency and reduce programming complexity. Third, we propose an adaptive weighted coefficient to couple the transmitting and two-way wavefields, and thus THABC can suppress reflections from the inner and outer boundaries. Finally, THABC exhibits excellent absorbing performance with fewer absorbing layers.

The rest of this paper is organized as follows. First, we review the second-order fractional Laplacians viscoacoustic equation and the transmitting formula expression. Then, we apply an adaptive weighted coefficient for equalizing internal and external boundary reflections and depict the THABC calculation flow. After that, we present the numerical results of seismic wave simulations on 3D homogeneous and overthrust models to further verify the feasibility and effectiveness of THABC. Finally, we discuss the computation efficiency and sensitivity of THABC to quality factor *Q*.

2. Theory

2.1. Second-order constant-Q viscoacoustic equation

Xing and Zhu (2019) have proposed a second-order fractional Laplacians viscoacoustic equation (Eq. (1)). It has drawn much attention because of its concise mathematical form and capacity to describe the frequency-independent Q behavior within all frequency bands (Wang et al., 2022). Particularly, Eq. (1) has the capacity to effectively decouple the effect of the amplitude decay and phase dispersion (Zhu and Harris, 2014), benefiting modeling and imaging applications.

$$\frac{1}{c^2} \frac{\partial^2 P_1}{\partial t^2} - \nabla^2 P_1 = \left(\gamma \frac{\omega_0}{c} \left(- \nabla^2 \right)^{1/2} - \gamma \frac{c}{\omega_0} \left(- \nabla^2 \right)^{3/2} \right) P_1 + \left(-\frac{\pi \gamma}{c} \left(- \nabla^2 \right)^{1/2} + \pi \gamma^2 \frac{1}{\omega_0} \nabla^2 \right) \frac{\partial}{\partial t} P_1, \tag{1}$$

ficiency over the conventional PML method. Another factor that plays a key role in boundary elimination is the weighted coefficient between the one-way and two-way wave equations. Liu and Sen (2018) presented an exponentially weighted coefficient to couple the boundary and central wavefields. This process can mitigate the inner boundary reflections but ignores the outer boundary reflections. Xie et al. (2020) also developed an effective HHABC with a cosine-type weighted coefficient. Currently, HABC has been rapidly developed and is widely used in seismic simulations (Zhao et al., 2014; Liu and He, 2015; Takekawa and Mikada, 2016; Liu et al., 2017; Wang and Liu, 2017; Xue et al., 2018).

In this paper, we aim to develop a new HABC based on a transmitting formula (refer to THABC) for second-order wave equations. More specifically, we devote our boundary to 3D viscoacoustic simulations involving fractional Laplacians. The proposed THABC benefits from the following advantages. First, compared with PML or CPML, THABC is especially suitable for second-order wave equations and does not require auxiliary variables or equations. Second, HHABC needs internal wavefields at the

where ∇^2 and P_1 represent the Laplacians and pressure wavefield, respectively. $\gamma=\frac{1}{\pi}\mathrm{arctan}\left(\frac{1}{Q}\right)$ and $c=c_0\cos(\pi\gamma/2)$, where c_0 is defined as the reference phase velocity at the reference frequency ω_0 . Due to containing fractional Laplacians in Eq. (1), the pseudospectral method is widely applied to solve fractional Laplacian operators (Zhu and Harris, 2014; Wang et al., 2018, 2019c), expressed as

$$\left(-\nabla^{2}\right)^{x}P_{1} = F^{-1}\left\{\left(k^{2}\right)^{x}F[P_{1}]\right\},$$
 (2)

$$\left(-\nabla^{2}\right)^{x}\frac{\partial}{\partial t}P_{1} = F^{-1}\left\{\left(k^{2}\right)^{x}F\left[\frac{\partial}{\partial t}P_{1}\right]\right\},\tag{3}$$

where F and F^{-1} denote the forward and reverse Fourier transforms, respectively. The finite difference scheme is utilized to calculate temporal derivatives. Therefore, Eq. (1) can be expressed as

$$P_{1}^{t+1} = 2P_{1}^{t} - P_{1}^{t-1} + dt^{2}c^{2} \begin{pmatrix} -F^{-1}\left\{\left(k^{2}\right)^{1}F\left[P_{1}^{t}\right]\right\} + \\ \gamma \frac{\omega_{0}}{c}F^{-1}\left\{\left(k^{2}\right)^{1/2}F\left[P_{1}^{t}\right]\right\} - \gamma \frac{c}{\omega_{0}}F^{-1}\left\{\left(k^{2}\right)^{3/2}F\left[P_{1}^{t}\right]\right\} - \\ \frac{\pi\gamma}{c}F^{-1}\left\{\left(k^{2}\right)^{1/2}F\left[\frac{\partial}{\partial t}P_{1}^{t}\right]\right\} - \pi\gamma^{2}\frac{1}{\omega_{0}}F^{-1}\left\{\left(k^{2}\right)^{1}F\left[\frac{\partial}{\partial t}P_{1}^{t}\right]\right\} \end{pmatrix}.$$

$$(4)$$

2.2. Transmitting boundary

The transmitting equation's expression is another key element of THABC. Based on the multiple transmission theory, the unified transmission formula in the *x*-direction boundary can be expressed as (Liao et al., 1984)

$$P_{2}(t + \Delta t, x, y, z) \approx \sum_{k=1}^{N} (-1)^{k+1} C_{k}^{N} P_{2}(t - (k-1)\Delta t, x - kc_{0}\Delta t, y, z),$$
(5)

where (x,y,z) is the spatial position, t refers to the temporal position, Δt represents the time step, N is the transmitting order $(N \ge 2)$ positively related to the absorbing effect of boundary reflections (N = 2 in this paper). $C_k^N = \frac{N!}{(N-k)!k!}$ and P_2 represent the second-order coefficient and transmitting wave wavefield, respectively.

Equation (5) can transmit incident waves out of the artificial boundary to avoid boundary reflections. However, it cannot be used for discrete numerical calculations and must be expressed discretely. Near the boundary, the distance between nodes perpendicular to the boundary is taken as a constant. Using the quadratic interpolation formula, Eq. (5) can be written as

$$P_2(t + \Delta t, x, y, z) \approx \sum_{k=1}^{N} (-1)^{k+1} C_k^N \mathbf{T}^k \mathbf{U}_{,}^k$$
 (6)

where \mathbf{T}^{k} , \mathbf{U}^{k} respectively represent the recursive coefficient and wavefield matrixes, written as (e.g., left boundary surface)

$$\begin{array}{l} t_1 = (2 - c_0 \Delta t/dx)(1 - c_0 \Delta t/dx)/2 \\ t_2 = (c_0 \Delta t/dx)(2 - c_0 \Delta t/dx) & k \geq 2 \,, \\ t_3 = (c_0 \Delta t/dx)(c_0 \Delta t/dx - 1)/2 \end{array} \tag{9}$$

and

$$u_{i,j} = P_2(t - (j-1)\Delta t, x - (i-1)dx), \tag{10}$$

where *x* and *dx* represent the space step in the *x*-direction and the coordinate of the boundary node, respectively. *i* and *j* represent the time and spatially-dependent variables, respectively.

As stated above, Eq. (6) can obtain the boundary wavefields using only wavefields at the current and last time steps.

2.3. Weighted coefficient

Because of the difference between the viscoacoustic equation and the transmitting formula, the abrupt variation between the physical domain and the boundary will inevitably cause boundary reflections. Hence, it is necessary to introduce a weighted coefficient to smooth the transition of different wavefields. Although a linear weighted coefficient (Liu and Sen, 2010) can be applied to eliminate boundary reflections, the coupling between the transmitting and viscoacoustic wavefields is not optimal. Liu and Sen (2018) enhanced the absorbing effect of the HABC by presenting a single-exponential weighted coefficient ω_1 (Eq. (11)) to solve the inner boundary reflections effectively; however, such an approach still cannot address the problem of outer boundary reflections. Along the same line, Xie et al. (2020) deformed ω_1 to obtain a single-exponential weighted coefficient ω_2 (as shown in Eq. (12)) to

$$\mathbf{T}^{k} = \begin{cases} [t_{1}, t_{2}, t_{3}, \cdots, t_{2k+1}] = [t_{1}, t_{2}, t_{3}] & k = 1 \\ [t_{1}, t_{2}, t_{3}] \begin{bmatrix} t_{k-1,1} & t_{k-1,2} & t_{k-1,3} \dots & t_{k-1,2k-1} & 0 & 0 \\ 0 & t_{k-1,1} & t_{k-1,2} & t_{k-1,3} \dots & t_{k-1,2k-1} & 0 \\ 0 & 0 & t_{k-1,1} & t_{k-1,2} & t_{k-1,3} \dots & t_{k-1,2k-1} \end{bmatrix} & k \ge 2 \end{cases},$$

$$(7)$$

and

where

 $\mathbf{U}^{k} = [u_{1,j}, u_{2,j}, u_{3,j}, \cdots, u_{2j+1,j}], \tag{8}$

suppress reflections at the outer boundary, but its absorbing capacity of internal boundary reflections is weak. Because a single-exponential weighted coefficient cannot simultaneously suppress internal and external boundary reflections, we propose an adaptive weighted coefficient (Eq. (13)) to better balance the internal and external reflected energy by effectively combining ω_1 and ω_2 .

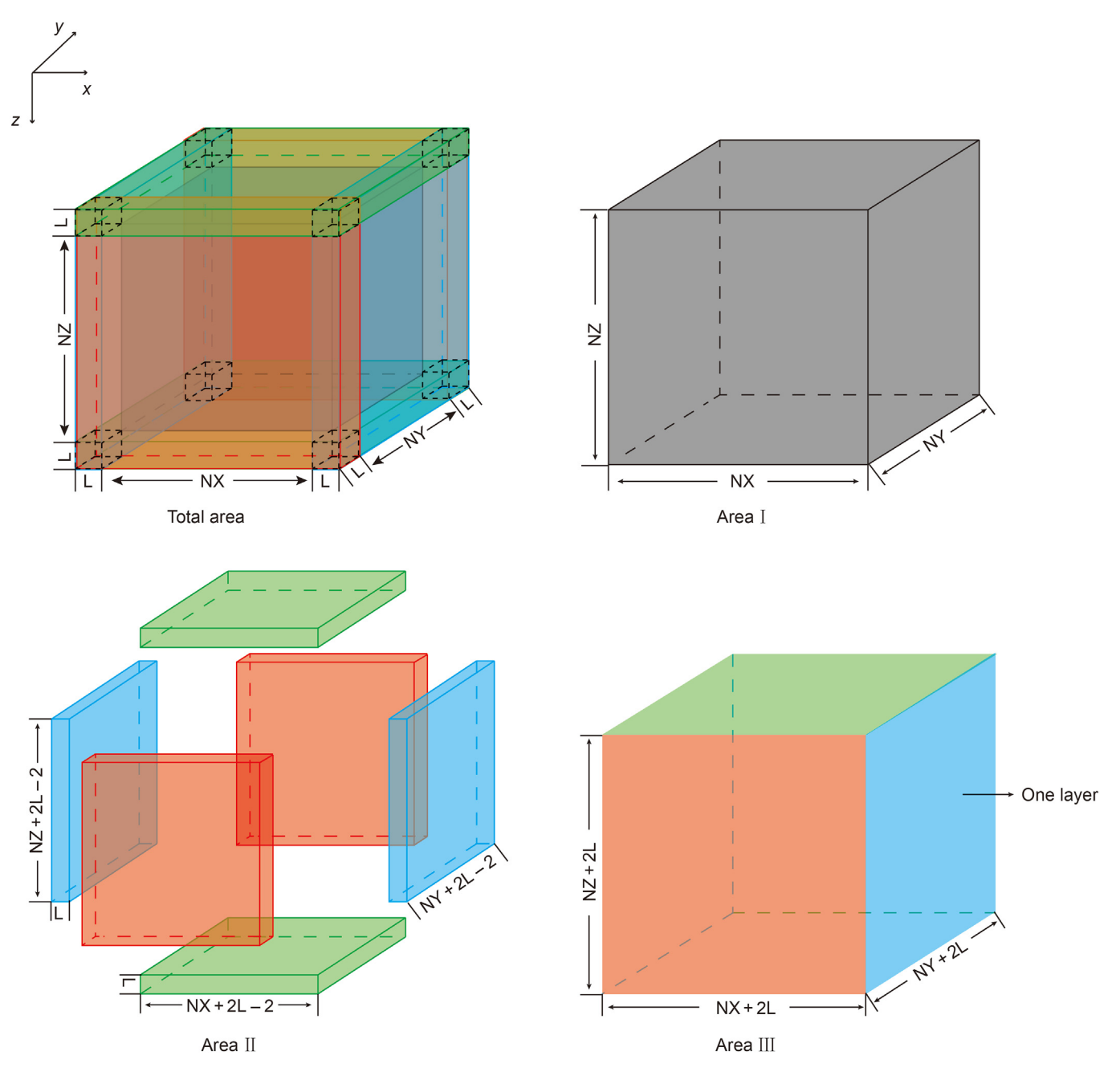


Fig. 1. The computing region of THABC in a 3D numerical simulation.

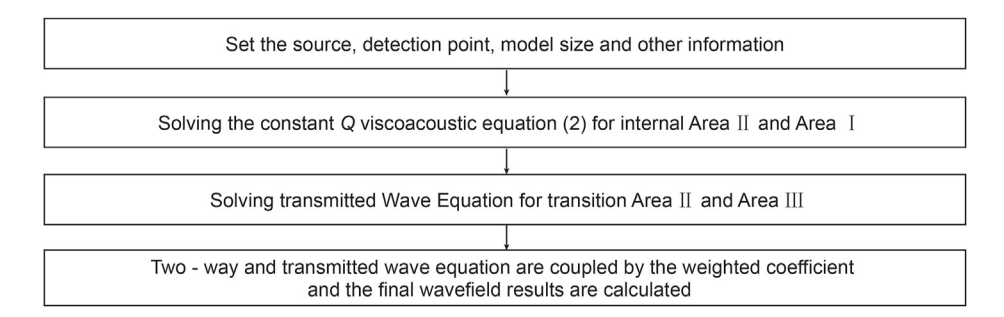


Fig. 2. THABC flow chart.

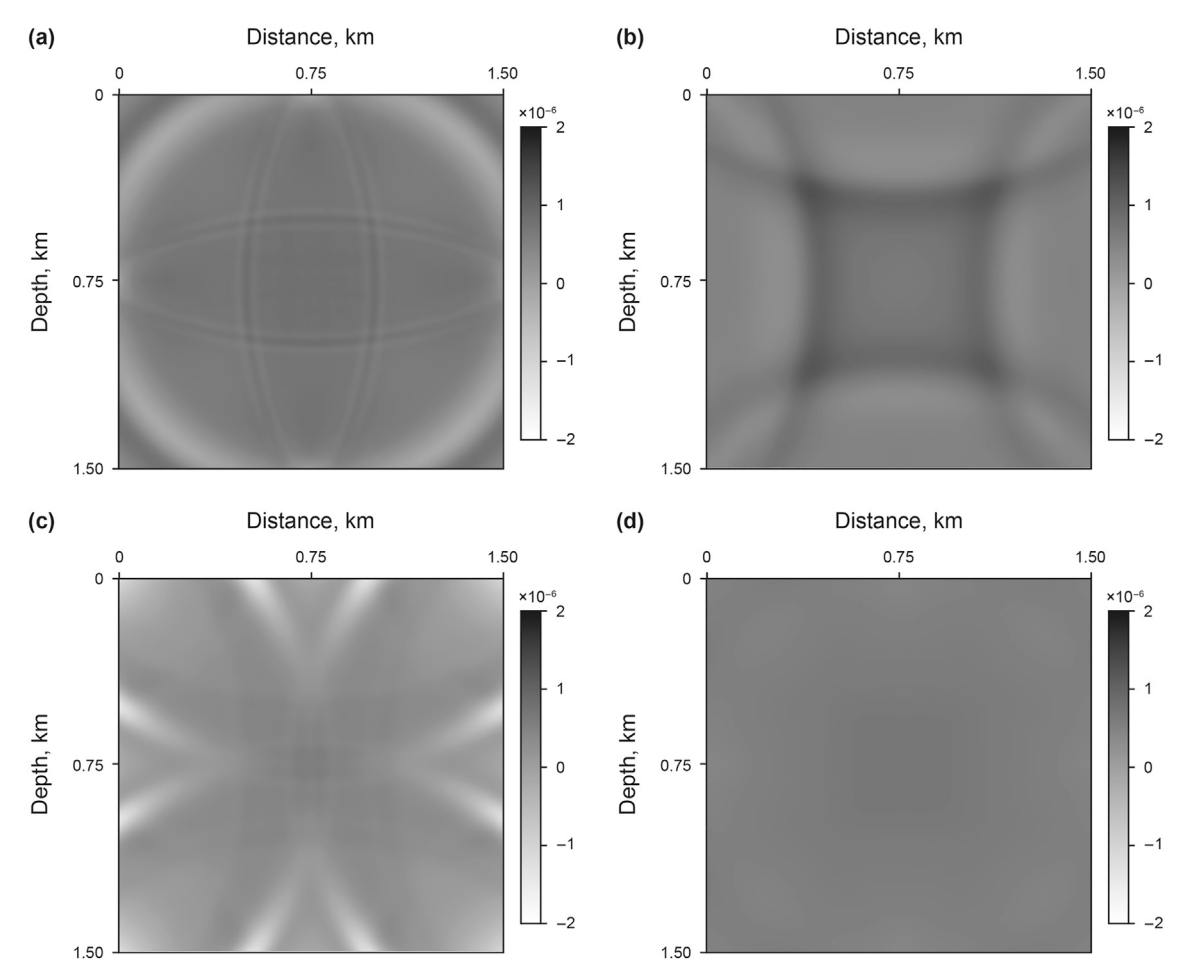


Fig. 3. 2D wavefield snapshot slices of 3D snapshots with different weighted coefficients (t = 600 ms, y = 750 m).

$$\omega_1 = \left(\frac{L - ix}{L}\right)^b \quad ix \in [0, L), \tag{11}$$

$$\omega_2 = 1 - \left(\frac{ix}{L}\right)^b \quad ix \in [0, L), \tag{12}$$

$$\begin{cases} k = \frac{ix}{L} & ix \in [0, L), \\ \omega = k\omega_1 + (1 - k)\omega_2 \end{cases}$$
 (13)

where ix and L represent the spatial position in the x-direction and the boundary width of the transition, respectively; $b=1.0+0.15\times L$, and k is the variable factor of the exponential function. Eq. (13) can automatically adjust the specific coupling ratio of the different single-exponential weighted coefficient according to the spatial position ix. Therefore, it can effectively balance the reflected energy generated from internal and external boundaries.

2.4. Numerical implementation

Fig. 1 depicts the computing region of THABC in a 3D numerical simulation. In Fig. 1, the size of the total area is $(Nx + 2L) \times (Ny + 2L) \times (Nz + 2L)$, which can be divided into the following three parts:

Area I is the internal domain or computation-domain (equal to

the real model) with the size of $Nx \times Ny \times Nz$. Area III is in the outermost layer with a thickness of 1. The size of Area III is 2 \times ($(Nx+2L) \times (Ny+2L)+(Nx+2L) \times (Nz+2L)+(Ny+2L) \times (Nz+2L)$). Excluding Areas I and III, the rest is Area II.

Nx, *Ny*, *Nz* are the numbers of grid cells in the *x*-, *y*-, and *z*-directions, respectively. As shown in Fig. 2, our approach is implemented by following the procedures. First, we solve the second-order viscoacoustic equation in total area. Then, we solve the transmitting formula in *Area II* and *Area III*. Finally, an adaptive weighted coefficient in *Area II* couples the viscoacoustic and transmitting wavefields. Thus, we obtain the expression of the boundary wavefield at the *t* moment

$$P(t, x, y, z) = \omega P_2(t, x, y, z) + (1 - \omega) P_1(t, x, y, z). \tag{14}$$

It is worth noting that the implementation at the boundary edge and corner regions is different from that on the boundary surfaces. The absorbing regions can be divided into six surface regions, twelve edge regions and eight corner regions in the 3D case. The boundary surfaces only need to absorb the reflections from one direction. Since Eq. (14) can absorb the incident wave in a specific direction, reflections at the edge regions (such as the overlapping layers of the *x*- and *y*-directions) can be suppressed by calculating the boundary surfaces of two directions. The treatment of the corner regions (overlapping layers of three surfaces) is similar to that of the edge regions; the properties of the corner regions are superimposed onto three surface directions.

Numerical simulations without ABC and with THABC can be expressed in Algorithms 1 and 2, respectively. Comparing Algorithms 1 and 2, we find that THABC only needs an extra calculation step and updates the boundary wavefields in the original numerical simulation step. Therefore, THABC can be embedded in the second-order viscoacoustic equation codes without modifying the primary framework, promising for pseudo-spectral and spectral-element simulations where second-order wave equations are widely used (Basu and Chopra, 2004; Festa and Vilotte, 2005; Matzen, 2011).

Algorithm 1. 3D viscoacoustic numerical simulation without ABC

et al., 2017) to verify the feasibility and effectiveness of our proposed scheme. Note that we used the split PML proposed by Chen et al. (2017). More specifically, we approximated the power of fractional Laplacians to the integer order, then split PML formulation for the second-order equation frame is introduced (Chen et al., 2013; Yuan et al., 2014).

3.1. Homogeneous model

We conduct seismic modeling in a homogeneous viscoacoustic medium, mainly compare the absorbing performance with different boundary conditions and discuss the effects using various

Algorithm 1 3D viscoacoustic numerical simulation without ABC

```
Require: Simulation parameters

Output: Wavefields (P^{ii+1}) and common-gather (r)

while it < nt do

while i \in \text{total computing domain do}

compute the spatial derivatives (Lap) using the Fourier pseudospectral (PS)

method;

P^{ii+1} = 2P^{ii} - P^{ii-1} + Lap Eq.(4);

update wavefields and save common-gather (r);

End while

End while
```

Algorithm 2. 3D viscoacoustic numerical simulation with THABC

```
Algorithm 2 3D viscoacoustic numerical simulation with THABC
```

```
Require: Simulation parameters and weighted coefficient (\omega)

Output: Wavefields (P^{ii+1}) and common-gather (r)

while it < nt do

while i \in \text{total computing domain do}

compute the spatial derivatives (Lap) using the Fourier pseudospectral (PS) method;

P^{ii+1}(i) = 2P^{ii}(i) - P^{ii-1}(i) + Lap \quad \text{(Eq. 4)};

while j \in \text{Area II & Area III do}

p_2^{ii+1}(j) \approx \sum_{k=1}^{2} (-1)^{k+1} C_k^N T^k U^k \quad \text{(Eq. 6)};

P^{ii+1}(j) = \omega p_2^{ii+1}(j) + (1-\omega)P^{ii+1}(j) \quad \text{(Eq. 14)};

End while

update wavefields and save common-gather (r);

End while

End while
```

3. Numerical experiments

In this section, we first compare the absorbing performance of THABC with different weighted coefficients. Then, we perform numerical simulation on 3D homogeneous and overthrust model using the proposed THABC, existing HHABC, and split PML (Chen

weighted coefficients. Simulations are performed at a reference velocity of 3000 m/s, and the quality factor Q is 50. The model contains $150 \times 150 \times 150$ cells with a uniform grid spacing of 10 m and 30 absorbing layers. A 30 Hz Ricker wavelet is at the model's center, and 150 receivers are at each grid point at x = 750 m and z = 300 m. The maximum excitation time is 1.2 s and the sampling

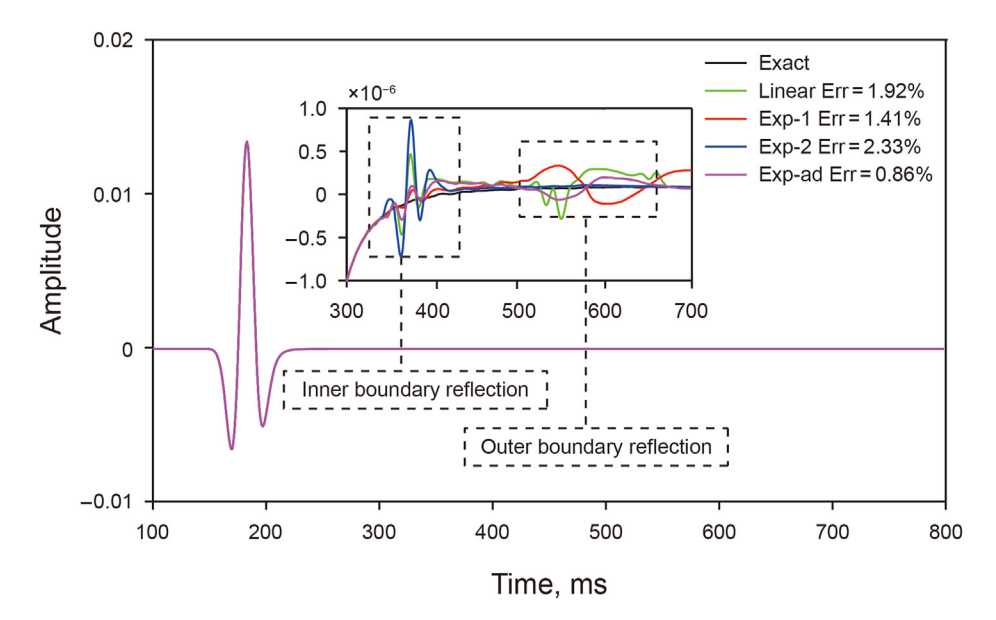


Fig. 4. Simulated seismograms with different weighted coefficients (x = 750 m, y = 750 m, z = 300 m).

interval is 1 ms.

In the first test, we compare the effectiveness with different weighted coefficients. Fig. 3 shows 2D slices of 3D snapshots at 600 ms. In detail, Fig. 3a-d correspond to the linear, exponential type 1 (Eq. (11)), the exponential type 2 (Eq. (12)), and the adaptive (Eq. (13)) schemes, respectively. In Fig. 3, we find that boundary reflections with different intensities exist in the slices of linear and single-exponential weighted coefficients, whereas inconspicuous boundary reflections can be observed in the adaptive weighted coefficient scheme. We obtain clear observations by displaying the portion of seismograms at x = 750 m, y = 750 m, and z = 300 m in Fig. 4, where the local zoomed-in sections at 300-700 ms are extracted. The black line represents the exact solution performed in an extended model without boundary reflections. The green, red, blue, and pink lines represent linear, exponential type 1, exponential type 2, and the proposed adaptive schemes, respectively. The total relative errors between the weighted coefficients and the exact solution are shown on the right side of the legend. Fig. 4 exhibits two prominent peaks (marked by boxes with a dotted line) corresponding to the reflections generated by the inner and outer boundaries of the transition regions. Notably, we can observe distinct boundary reflections in the green line, indicating that the linear weighted coefficient is unsatisfying on suppressing boundary reflections. The blue and red lines show the obvious reflections generated at the inner and outer boundaries, respectively. These phenomena suggest that the single-exponential weighted coefficients cannot effectively couple two different wave equations. From another perspective, the adaptive weighted coefficient has the advantages of single-exponential types 1 and 2. Thus, considering the overall absorbing effect of the inner and outer boundaries, we utilize the adaptive weighted coefficient to perform the following tests.

As stated above, the proposed THABC performs than the existing schemes with the same absorbing layers. The 3D homogeneous model further verifies this superiority. In Fig. 5, from top to bottom, the snapshots correspond to the without absorbing boundary, the split PML (hereinafter referred to as PML), the HHABC, and the THABC, respectively. The first column represents the 3D snapshots at 350 ms, the second column corresponds to 500 ms, and the third column highlights the 2D wavefield slices at t=500 ms and

y = 750 m. Specifically, at 350 ms when a seismic wave arrives at the boundary, it travels back into the physical domain because the boundary is untreated; by contrast, the boundary reflections cannot be observed in Fig. 5b-d. At 500 ms when the seismic wave has fully traveled through the calculated regions, serious false reflections occur in Fig. 5e and i. Obviously, PML boundary cannot reduce boundary reflections effectively (as shown in Fig. 5f and j), indicating that this scheme needs more absorbing layers. Although HHABC can absorb most boundary reflections, visible faint pseudooscillations still occur in Fig. 5g and k. Differently, it is challenging to observe the boundary reflections under the same gain control in Fig. 5h and l, indicating a prominent absorbing effect of THABC. Fig. 6 sketches the common-gathers with different boundary conditions, and we cut off the direct wave to better investigate the boundary reflections. Fig. 6a-d correspond to the exact solution, without absorbing boundary, HHABC, and THABC, respectively. Note that we display Fig. 6a, c and d in the same amplitude range and observe substantial high-energy false reflections in Fig. 6b due to the untreated boundary. In Fig. 6c, the false reflections of HHABC are relatively feeble, and only the spurious responses before 750 ms could be observed. Differently, THABC generates a similar commongather as the exact solution. To understand the discrepancies in accuracy with different absorbing methods in detail, seismograms at 100-800 ms are shown in Fig. 7. We also display a local zoomedin section of 300-700 ms for clearer observation. Fig. 7a-c correspond to 10, 20 and 30 layers where the black, red, blue and green lines denote the exact solution, HHABC, PML and THABC, respectively. Since the boundary reflections of PML are strong, we multiply them by 0.1, 0.15, and 0.25 in the zoomed-in box. In Fig. 7, the boundary reflections of PML and HHABC are obvious, whereas THABC (green lines) is closer to the exact solution. For quantify, we utilize the root mean square error (RMS) to quantitatively evaluate the accuracy of different boundary conditions shown in Fig. 8 where Fig. 8a-c represent 10, 20 and 30 layers, respectively. The RMS equation can be expressed as

$$E_{\text{rms}}(x, y, z) = \sqrt{\frac{\sum_{i t=0}^{nt} \left(\left(P_{\text{cal}} \left(x, y, z, it \right) - P_{\text{ref}} \left(x, y, z, it \right) \right)^{2}}{nt}}, \quad (15)$$

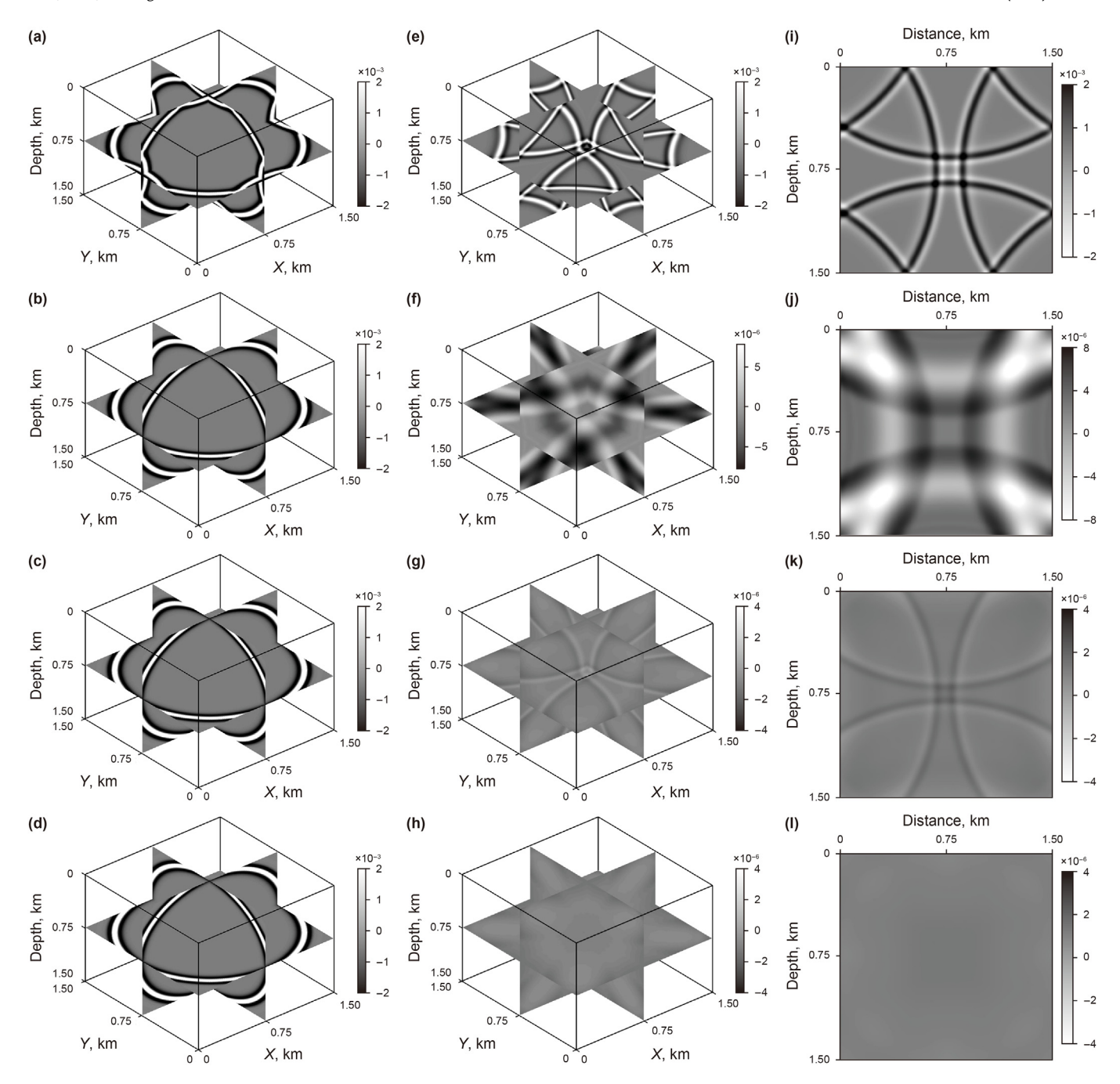


Fig. 5. Wavefield snapshots of different boundary conditions.

where $P_{\rm ref}$ represents the wavefield of the exact solution, and $P_{\rm cal}$ is the wavefield obtained by different boundary conditions. In Fig. 8, the lowest *RMS* of THABC also confirms its superiority in suppressing boundary reflections.

3.2. Free surface application

Here, we evaluate the applicability of THABC when a free surface is present. The velocity model and numerical simulation parameters are the same as the homogeneous model, except that the absorbing layers on the upper boundary are replaced by the free surface. We implement the free surface via the mirror-image inverse-symmetry boundary condition (Graves, 1996). Fig. 9a—d

shows snapshots at 0.2, 0.3, 0.4, and 0.7s, obviously, the wavefield energy propagates steadily, except for the free boundary reflections, the reflections can be well absorbed. Fig. 10 shows the energy decay curve with different ABCs where the black, blue, and red lines represent THABC, HHABC and PML, respectively. The black line decays the fastest, indicating that THABC can effectively suppress boundary reflections when the free surface is present. We further extended the simulation to 20 s to further evaluate the stability of THABC in large-time numerical simulations, and use a regularizing operator (Liao et al., 2002) to avoid the zero-frequency drift. As the energy attenuation curves show (Fig. 11), the THABC is still stable even for 20 s.

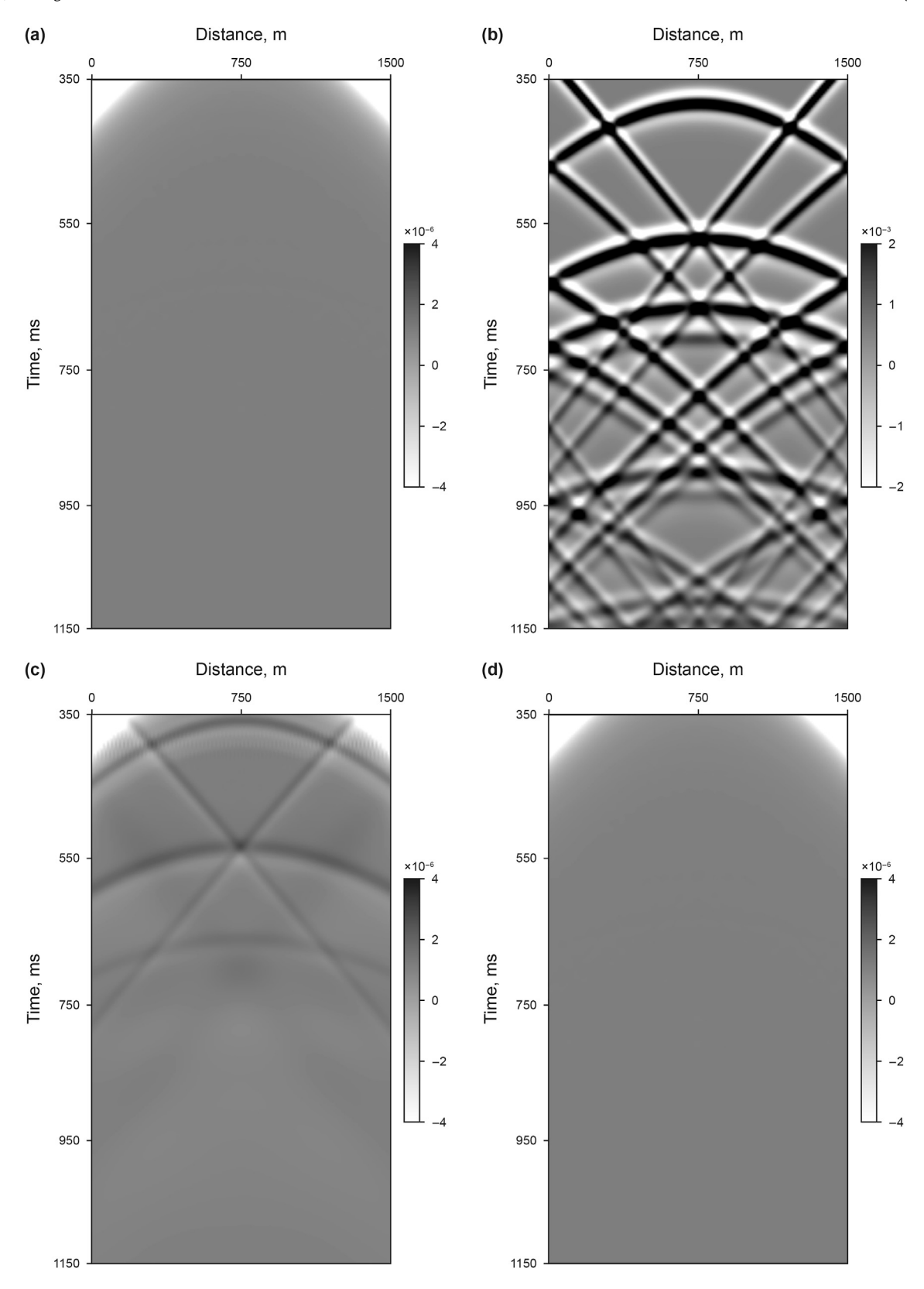
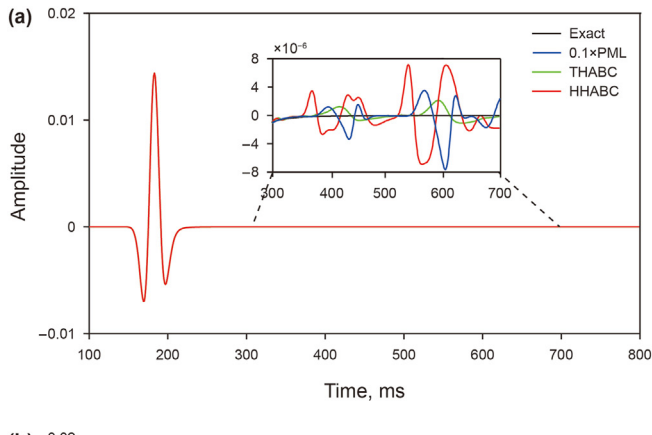


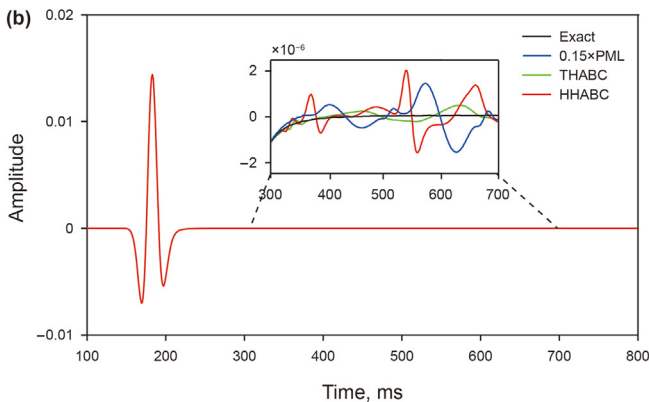
Fig. 6. Common-gathers without direct wave.

3.3. 3D overthrust model

We verify the effectiveness of THABC for the complex medium

by performing 3D seismic modeling on the overthrust model. Fig. 12 denotes the velocity model, numerically discretized into $200 \times 200 \times 100$ grid points with a uniform grid spacing of 10 m.





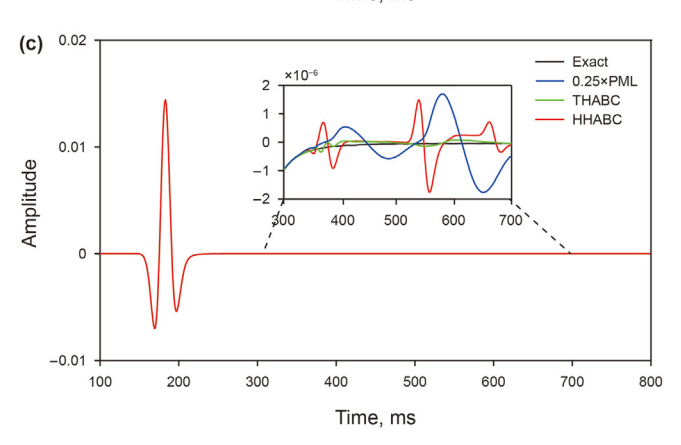
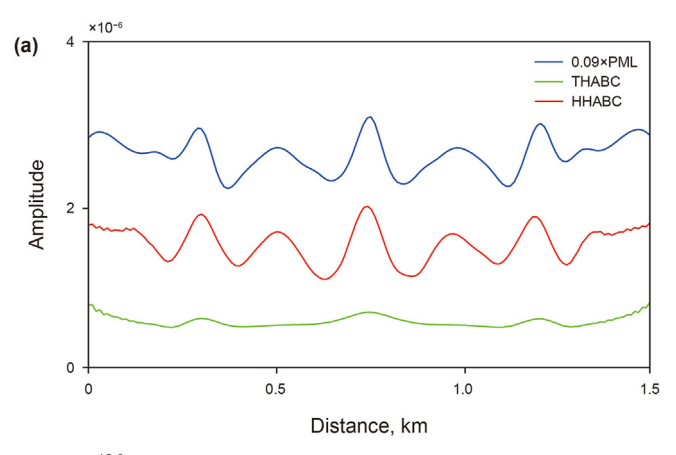
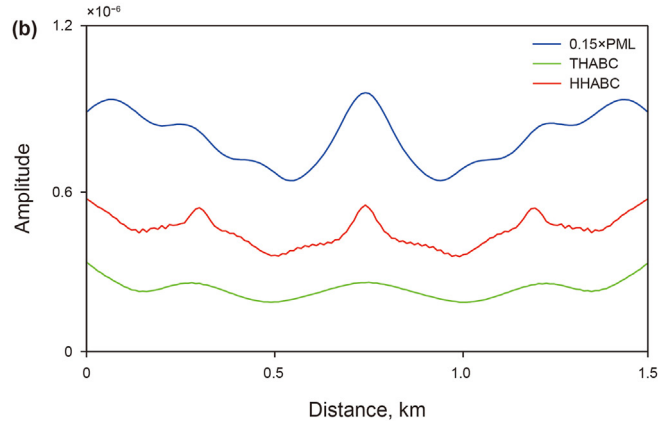


Fig. 7. Common-gathers for the homogeneous model with different ABCs at ($x=750~{\rm m},\,y=750~{\rm m},\,z=300~{\rm m}$).

Likewise, the Q model is built from the velocity model with an empirical function of $Q=3.516(c_0/1000)^{2.2}$ (Li, 1993), with a wide velocity range and contains a high attenuation domain. A 25 Hz Ricker wavelet is used as the source at x=1000 m, y=1000 m, and z=80 m. In total, 10000 receivers are uniformly located at a depth of 80 m. The simulation time is 1.5 s, with a 1 ms time step, and the absorbing boundary are 30 layers.

Fig. 13 shows snapshots of different absorbing conditions, in which the left and right columns correspond to 300 and 1300 ms, respectively. From top to bottom, the boundary of each row is without absorbing boundary, PML, HHABC and THACB, respectively. Fig. 14 shows that the amplitudes in the four cases are highly similar when the wave starts to propagate. At 1300 ms, the wavefield of the PML boundary condition exhibits strong boundary reflections, indicating that the absorbing effect of the PML is dissatisfying when the absorbing layers are insufficient. Obviously, HHABC only corresponds





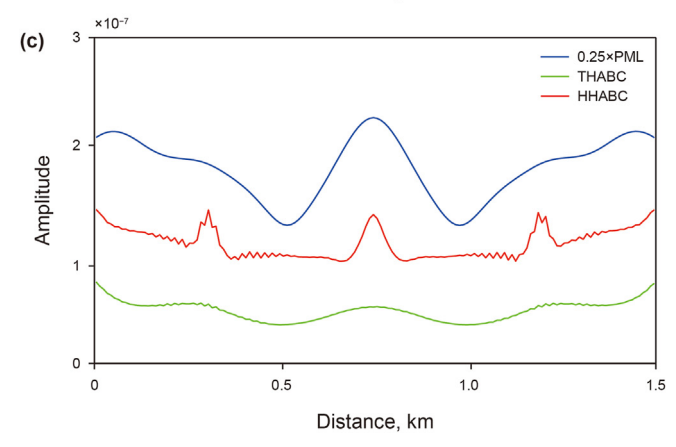


Fig. 8. RMS curve of common-gathers for the 3D homogeneous model.

to slight reflection energy, better than PML, whereas THABC suppresses the boundary reflections effectively. Fig. 14 shows the 3D common-gathers, in which Figs. 14a—d correspond to the without absorbing boundary, PML, HHABC, and THABC, respectively. All common-gathers are displayed in the same amplitude range. As indicated in Fig. 14a, severe false events are produced without boundary conditions, contaminating the effective wavefields and affecting the authenticity of the subsequent processing. Although the PML boundary condition suppresses most false reflections, evident boundary reflections can still be observed in Fig. 14b. The commongathers of the two HABC exhibit a remarkable absorbing effect and no obvious false reflections can be observed (as shown in Fig. 14c and d). We further compare the absorbing effects of the two hybrid absorbing boundaries by extracting the trace at x = 880 m, y = 1980 m, and z = 80 m. As shown in Fig. 15, the red, green and black lines

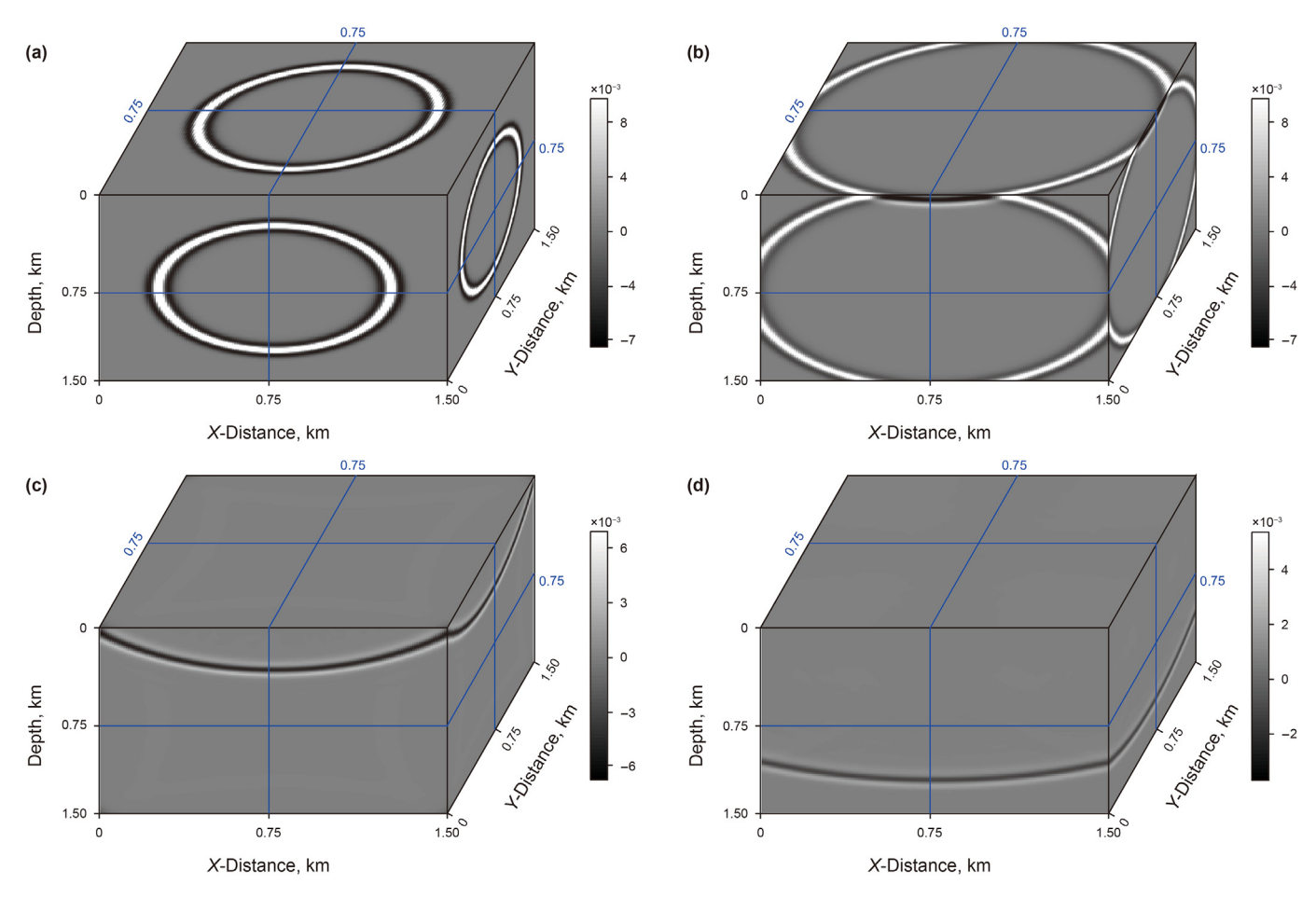


Fig. 9. Wavefields of THABC when considering the free surface.

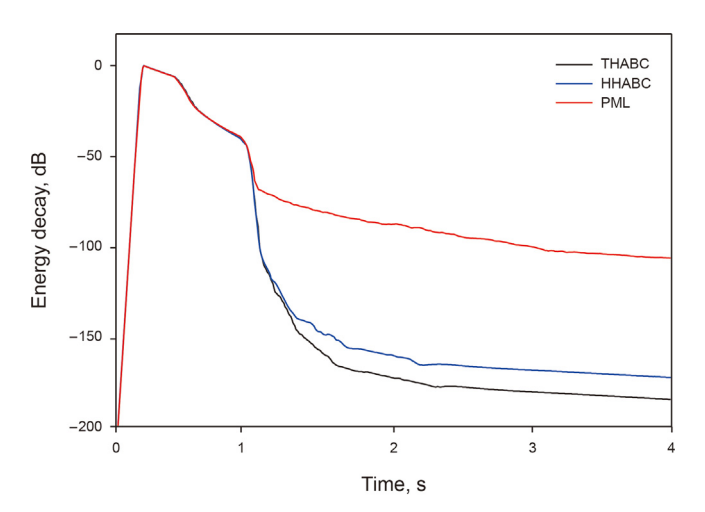


Fig. 10. Energy decay with different ABCs for homogeneous model when considering the free surface.

represent the exact solution, HTABC and HHABC, respectively. In the zoomed-in box, the blue line marks the absolute error between the exact solution and THABC (ERR1), and the pink line represents the absolute error between the exact solution and HHABC (ERR2). It is prominent that ERR1 is less than ERR2, illustrating that THABC has exerted a better absorbing effect in the 3D viscoacoustic complex heterogeneous media.

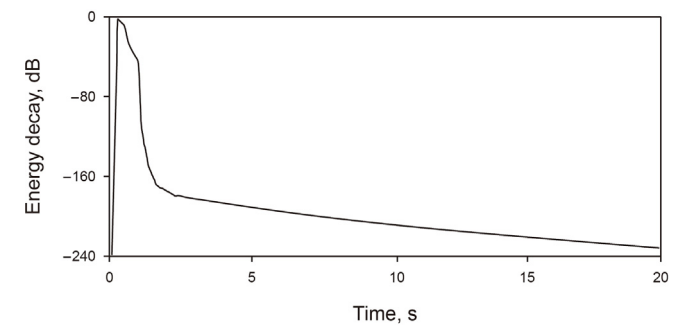


Fig. 11. Energy decay of THABC for 20 s simulation.

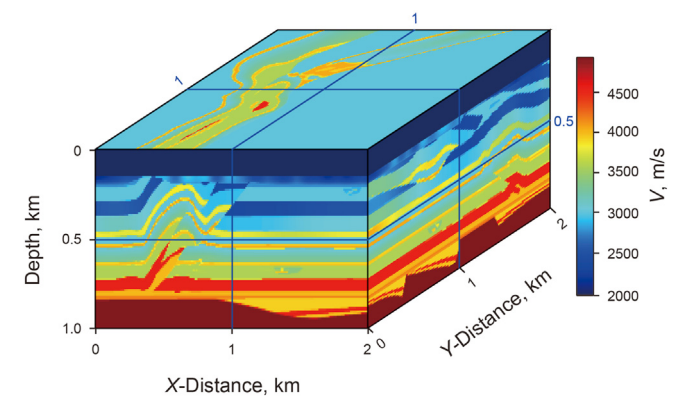


Fig. 12. 3D overthrust velocity model.

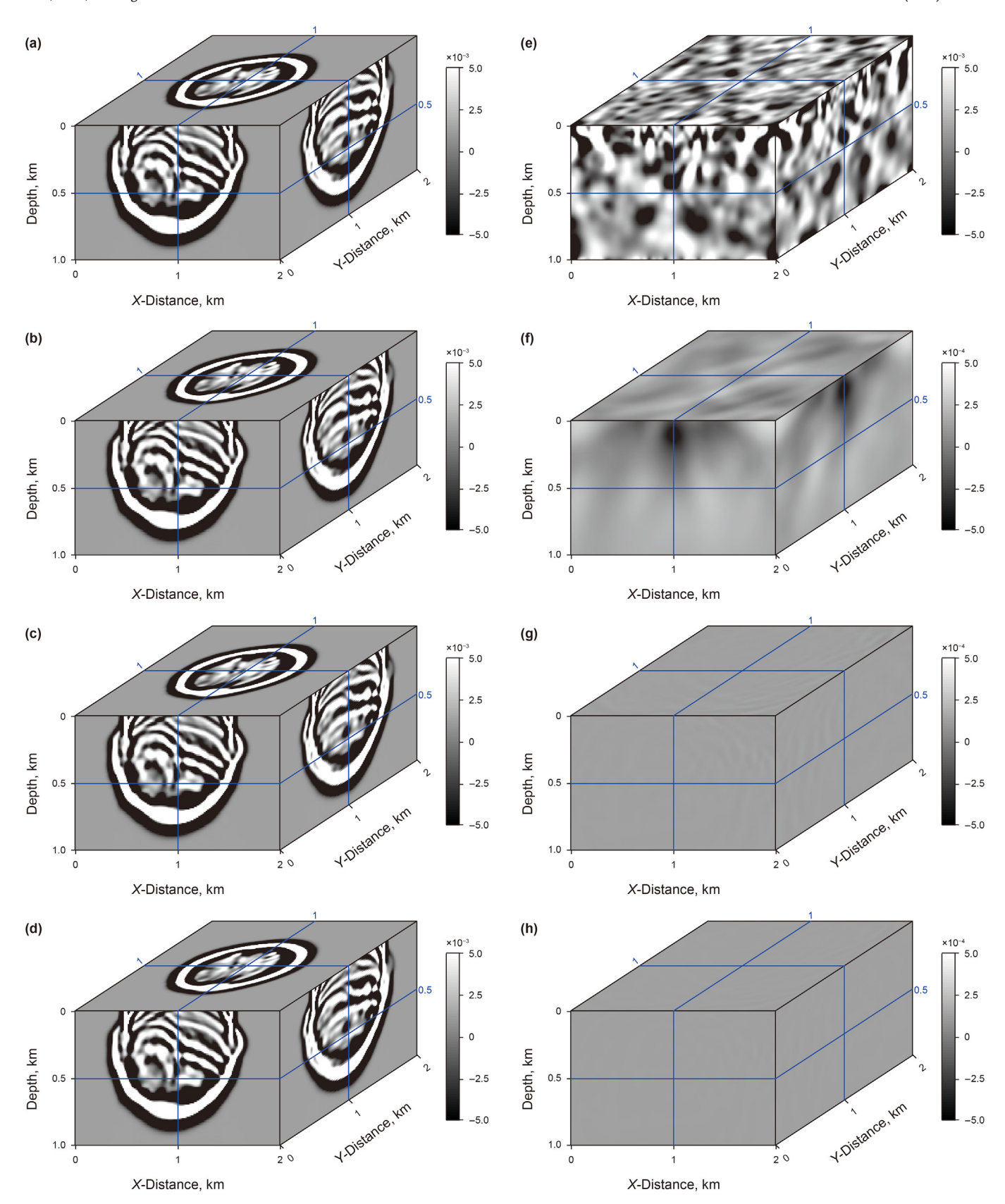


Fig. 13. 3D snapshots of the displacement field from viscoacoustic modeling with different boundary conditions.

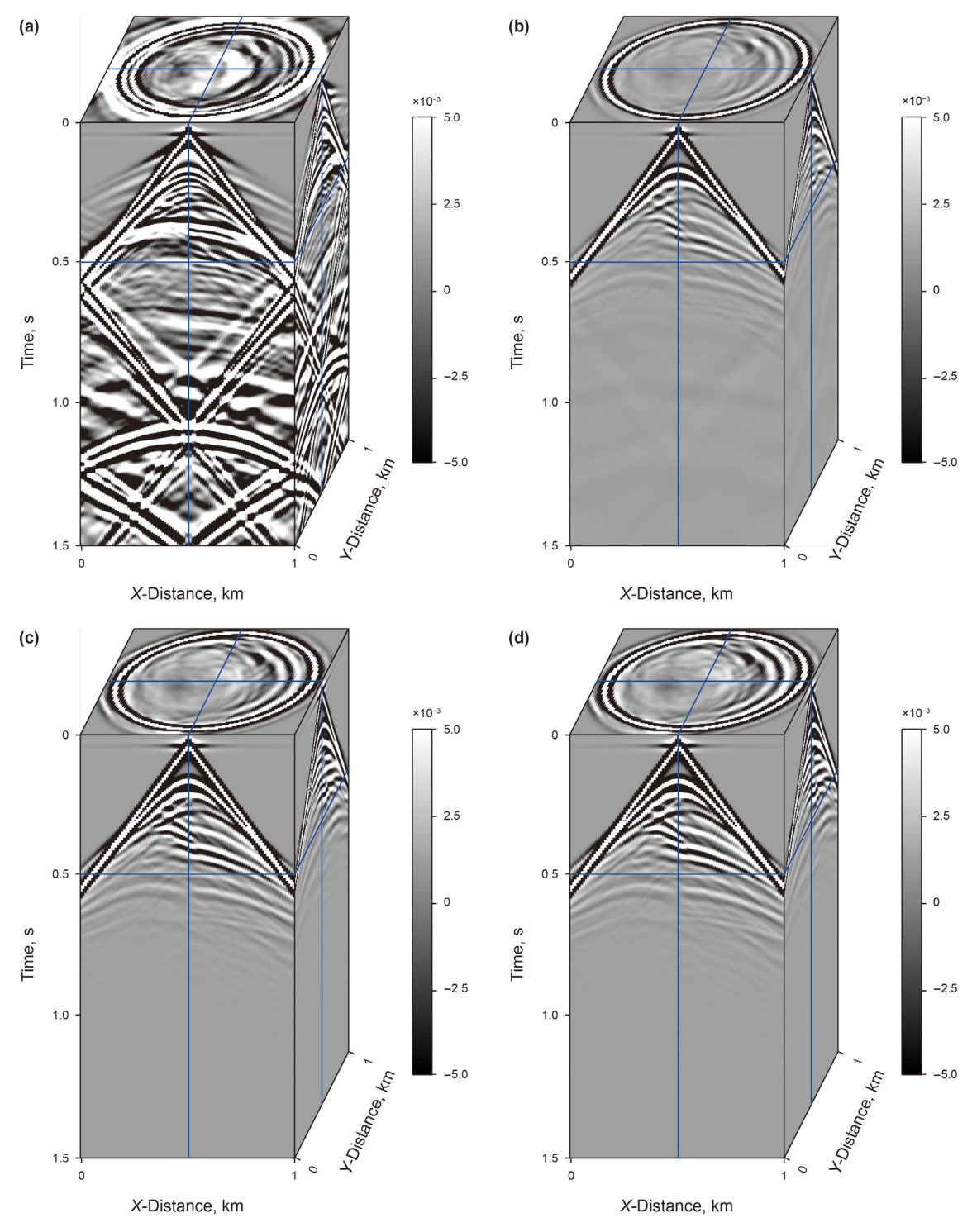


Fig. 14. Common-gathers for 3D overthrust model with different boundary conditions.

4. Discussion

4.1. Computation cost

In this section, we compare the computation cost of different absorbing conditions. All numerical examples are implemented using the Compute Unified Device Architecture (CUDA) programing on a Nvidia Geforce RTX 2080Ti. The model parameters are consistent with those in the homogeneous model except for the

absorbing layers. Table 1 shows the calculation time of different boundary conditions with 20 absorbing layers. In Table 1, the PML calculation time is the longest, that of THABC is the shortest, and HHABC is slightly higher than THABC. Fig. 16 shows the energy decay curve in the physical domain, in which the blue, black and red lines represent PML, HHABC, and THABC, respectively. The waves leave the physical domain between 350 ms and 700 ms, as indicated by the steep decay in Fig. 16. All remaining energy, thereafter, is not only spurious reflections but also indicators of the boundary

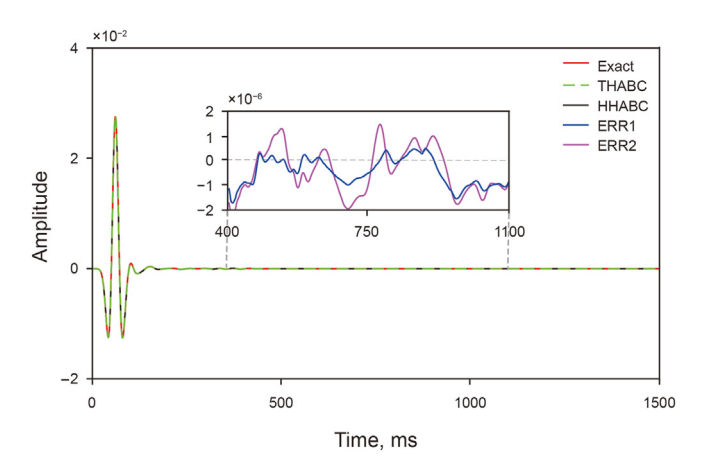


Fig. 15. Absolute error curves between different ABCs and the exact solution (x = 880 m, y = 1980 m, z = 80 m).

Table 1The calculation time of different boundary conditions with the same layer thickness.

Boundary	Weighted	Layer	Calculation	Propagation
condition	coefficient	thickness	time, s	time, s
THABC	adaptive	20	49.08	4 4
HHABC	adaptive	20	53.24	
PML	_	20	68.86	4

condition's efficiency. Fig. 16 indicate that the PML energy curve only decreases to approximately -100 dB, indicating that more absorbing layers should be added in this scheme to enhance the absorbing effect. Strikingly, the energy of THABC is minimal in the physical domain and the energy curve decreases rapidly to approximately -220 dB. Furthermore, Table 1 shows that THABC can save 8.2% and 35.8% of the computational cost compared with HHABC and PML, respectively. Hence, the method proposed in this study enjoys a great advantage in absorbing effects and computational efficiency.

4.2. Code implementation

In addition to the absorbing effect and computational cost, the convenience of code implementation is also a vital indicator in evaluating ABC performance. Therefore, we briefly discuss code implementation for different boundary conditions. Due to the governing equation depending on the wave equation, PML requires overhauling revision of the existing finite-difference method, finite element method, and pseudo-spectral methods (Zhuang et al., 2020). Because Eq. (1) contains fractional Laplacians, it is difficult to transform the viscoacoustic wave equation into a new secondorder partial differential equation in CPML. Meanwhile, CPML is harder to be directly applied to the second-order wave equation because it needs to introduce auxiliary variables or equations (Duru and Kreiss, 2012; Ma et al., 2019). Such procedures would undoubtedly increase additional computation burdens and storage. The traditional HHABC needs to be calculated from the inside to the outside boundary. Therefore, it is inconvenient to CUDA programming, increasing the unnecessary computational complexity. By contrast, THABC refrains from rewriting the original modeling code and is convenient for implementing multithreaded calculations. Furthermore, HABC theoretically applies to most second-order

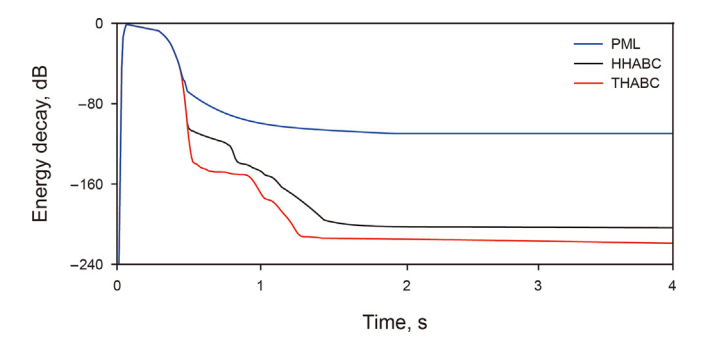


Fig. 16. Energy decay in the computational domain for homogeneous model with 20 absorbing layers.

equations (Liu and Sen, 2012), indicating that THABC has the same advantage in universality. Theoretically, THABC can be extended to elastic wave equations, and we will focus on it in the future.

4.3. Effect of different Q values

Quality factor Q should characterize the absorbing and attenuation characteristics of seismic waves propagated in underground media, and is one of the most significant parameters in viscoacoustic numerical simulations. Therefore, it is necessary to discuss the effects exerted by Q factor on different absorbing schemes. We conduct numerical modeling on 3D homogeneous models, in which the parameters are the same as those in previous homogeneous models but Q alters from infinity to 20. Fig. 17 shows 2D wavefield snapshot slices with different Q values at y = 750 m and t = 600 ms, in which all snapshots are shown with the same amplitude range. The left and right columns represent HHABC and THABC, respectively. Overall, the boundary reflections in the left column are stronger than those in the right, indicating that THABC has a better absorbing effect with different O values. From top to bottom, each row's quality factor O is infinity, 100, 50 and 20, respectively. Conspicuously, the boundary reflections are weaker as Q decreases because the medium's inelasticity attenuates the boundary reflections. We quantitatively express the absorbing effect of boundary reflections with different Q values by defining the boundary reflection energy intensity (LEI), representing a relative maximum error between THABC and the exact solution during the simulation time. The LEI equation can be expressed as

$$LEI(x,y,z) = \max_{\forall t \in [0,nt]} \left\{ 20\log_{10} \left\{ \frac{\left| P_{ref}(x,y,z,t) - P_{cal}(x,y,z,t) \right|}{\max_{\forall t \in [0,nt]} \left\{ \left| P_{ref}(x,y,z,it) \right| \right\}} \right\} \right\}, \tag{16}$$

where $P_{\rm ref}$ represents the exact solution. $P_{\rm cal}$ is the numerical solution based on THABC with different Q. The LEI curve is described in Fig. 18. It is remarkable that all LEI curves are highly similar for different Q values close to -90 dB, indicating that the maximum reflection energy is five to six orders smaller compared with the first arrival wave. Therefore, we suggest that quality factor Q exerts a relatively small influence on the absorbing performance of THABC.

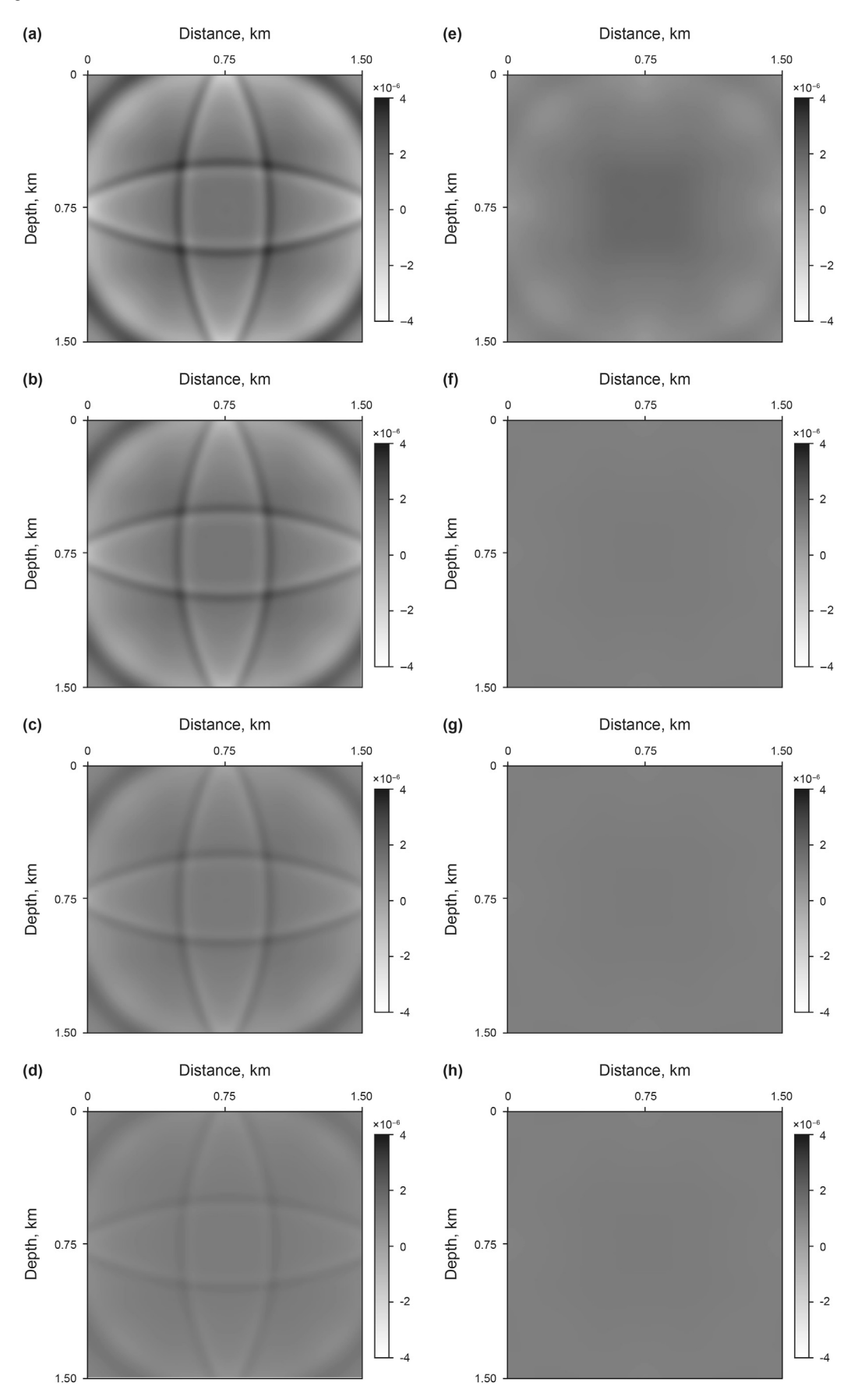


Fig. 17. 2D wavefield snapshot slices with different Q values at 600 ms

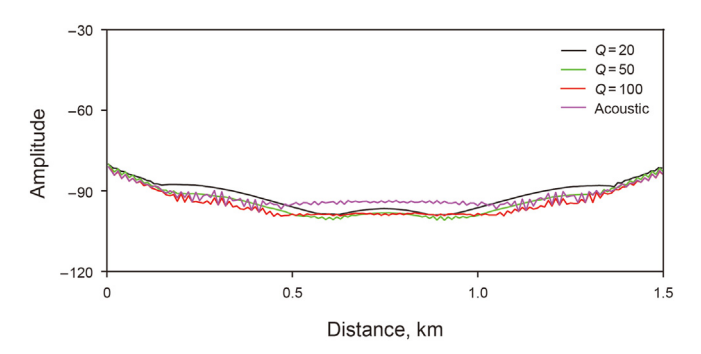


Fig. 18. LEI result curve with different Q

5. Conclusions

We have developed a THABC method for the second-order fractional Laplacian viscoacoustic wave equation. The proposed scheme enables us to suppress artificial boundary reflections in 3D viscoacoustic wavefields without rewriting the original wave equations or introducing additional auxiliary variables. The proposed scheme enjoys high computational efficiency since it only needs the current and last wavefields. Numerical experiments show that the proposed scheme exhibits excellent absorbing performance and computational efficiency. We anticipate that the proposed THABC will directly benefit high-precision imaging applications and the development of inversion in 3D attenuation media.

Acknowledgements

We thank the National Natural Science Foundation of China under Grant Nos. 41930431 and 41974116, Natural Science Foundation of Heilongjiang Province No. YQ2021D008, and CNPC Innovation Found No. 2021DQ02-0302 for supporting this work.

References

- Alford, R.M., Kelly, K.R., Boore, D.M., 1974. Accuracy of finite difference modeling of the acoustic wave equation. Geophysics 39 (6), 834–842. https://doi.org/10.1190/1.1440470.
- Basu, U., Chopra, A.K., 2004. Perfectly matched layers for transient elastodynamics of unbounded domains. Internat.j.numer.methods Engrg. 59 (8), 1039–1074. https://doi.org/10.1002/nme.896.
- Berenger, J.P., 1994. A perfectly matched layer for the absorbing of electromagnetic waves. J. Comput. Phys. 114 (2), 185–200. https://doi.org/10.1006/jcph.1994.1159.
- Cerjan, C., Kosloff, D., Kosloff, R., et al., 1985. A nonreflecting boundary condition for discrete acoustic and elastic wave equations. Geophysics 50 (4), 705–708. https://doi.org/10.1190/1.1441945.
- Chen, H.M., Zhou, H., Lin, H., Wang, H.X., 2013. Application of perfectly matched layer for scalar arbitrarily wide-angle wave equations. Geophysics 78 (1), T29–T39. https://doi.org/10.1190/geo2012-0062.1.
- Chen, H.M., Zhou, H., Xia, M., 2017. Efficiency improved scalar wave low-rank extrapolation with an effective perfectly matched layer. J. Geophys. Eng. 14 (1), 113–119. https://doi.org/10.1088/1742-2140/14/1/113.
- Chew, W.C., Weedon, W.H., 1994. A 3D perfectly matched medium from modified maxwell's equations with stretched coordinates. Microwave and Optical Techno. logy Lett. 7 (13), 599–604. https://doi.org/10.1002/mop.4650071304.
- Clayton, R., Engquist, B., 1977. Absorbing boundary conditions for acoustic and elastic wave equations. Bull. Seismol. Soc. Am. 67 (6), 1529–1540. https://doi.org/10.1007/BF02317997.
- Collino, F., Tsogka, C., 2001. Application of the perfectly matched absorbing layer model to the linear elastodynamic problem in anisotropic heterogeneous media. Geophysics 66 (1), 294–307. https://doi.org/10.1190/1.1444908.
- Duru, K., Kreiss, G., 2012. A well-posed and discretely stable perfectly matched layer for elastic wave equations in second order formulation. Commun. Comput. Phys. 11 (5), 1643–1672. https://doi.org/10.4208/cicp.120210.240511a.
- Festa, G., Vilotte, J.P., 2005. The Newmark scheme as velocity-stress time-staggering: an efficient PML implementation for spectral element simulations of elastodynamics. Geophys. J. Roy. Astron. Soc. 161 (3), 789–812. https://doi.org/ 10.1111/j.1365-246X.2005.02601.x.

Fornberg, B., 2012. The pseudospectral method: comparisons with finite differences for the elastic wave equation. Geophysics 52 (4), 483–501. https://doi.org/

- Graves, R.W., 1996. Simulating seismic wave propagation in 3D elastic media using staggered-grid finite differences. Bull. Seismol. Soc. Am. 86 (4), 1091–1106. https://doi.org/10.1016/0009-2541(96)00016-2.
- Heidari, A.H., Guddati, M.N., 2006. Highly accurate absorbing boundary conditions for wide-angle wave equations. Geophysics 71 (3), S85-S97. https://doi.org/ 10.1190/1.2192914.
- Higdon, R.L., 1986. Absorbing boundary conditions for difference approximations to the multi-dimensional wave equation. Math. Comput. 47 (176), 437–459. https://doi.org/10.2307/2008166.
- Higdon, R.L., 1987. Numerical absorbing boundary conditions for the wave equation. Math. Comput. 49 (179), 65–90. https://doi.org/10.1090/S0025-5718-1987-0890254-1
- Higdon, R.L., 1991. Absorbing boundary conditions for elastic waves. Geophysics 56 (2), 231–241. https://doi.org/10.1190/1.1443035.

 Khataniar, S., Peters, E.J., 1991. A comparison of the finite-difference and the finite-
- Khataniar, S., Peters, E.J., 1991. A comparison of the finite-difference and the finite-element methods for simulating unstable displacements. J. Pet. Sci. Eng. 5 (3), 205—218. https://doi.org/10.1016/0920-4105(91)90038-0.
- Komatitsch, D., Tromp, J., 2003. A perfectly matched layer absorbing boundary condition for the second-order seismic wave equation. Geophys. J. Int. 154 (1), 146–153. https://doi.org/10.1046/j.1365-246X.2003.01950.x.
- Kreiss, H.O., Oliger, J., 1972. Comparison of accurate methods for the integration of hyperbolic equations. Tellus 24 (3), 199–215. https://doi.org/10.1111/j.2153-3490.1972.tb01547.x.
- Kuzuoglu, M., Mittra, R., 1996. Frequency dependence of the constitutive parameters of causal perfectly matched anisotropic absorbers. IEEE Microw. Guid. Wave Lett. 6 (12), 447–449. https://doi.org/10.1109/75.544545.
- Li, Q.Z., 1993. High Resolution Seismic Data Processing. Petroleum Industry Press.
- Li, Y., Matar, O.B., 2010. Convolutional perfectly matched layer for elastic secondorder wave equation. J. Acoust. Soc. Am. 127 (3), 1318–1327. https://doi.org/ 10.1121/1.3290999.
- Li, C., Huang, J.P., Li, Z.C., et al., 2017. Regularized least-squares migration of simultaneous-source seismic data with adaptive singular spectrum analysis. Petrol. Sci. 14 (1), 61–74. https://doi.org/10.1007/s12182-016-0134-1.
- Liao, Z.P., Wong, H.L., Yang, B.P., et al., 1984. A transmitting boundary for transient wave analysis. Sci China Series A-Math Phys Astron. Technol Sci. 27 (10), 1063–1076. https://doi.org/10.1360/ya1984-27-10-1063.
- Liao, Z.P., Zhou, Z.H., Zhang, Y.H., 2002. Stable implementation of transmitting boundary in numerical simulation of wave motion. Chin. J. Geophys. 45 (4), 554–568. https://doi.org/10.3321/j.issn:0001-5733.2002.04.011.
- Liu, Y., Sen, M.K., 2010. A hybrid scheme for absorbing edge reflections in numerical modeling of wave propagation. Geophysics 75 (2), A1–A6. https://doi.org/ 10.1101/J.2026.47
- Liu, Y., Sen, M.K., 2012. A hybrid absorbing boundary condition for elastic staggered-grid modelling. Geophys. Prospect. 60 (6), 1114–1132. https://doi.org/10.1111/j.1365-2478.2011.01051.x.
- Liu, X., He, B.S., 2015. First-order hybrid absorbing boundary condition in VTI media elastic wave equation forward modeling. Coal Geol. China. 27, 59–63. https:// doi.org/10.3997/2214-4609.201601057.
- Liu, X., Liu, Y., Ren, Z.M., et al., 2017. Hybrid absorbing boundary condition for three-dimensional elastic wave modeling. Appl. Geophys. 14 (2), 270–278. https://doi.org/10.1007/s11770-017-0623-z.
- Liu, Y., Sen, M.K., 2018. An improved hybrid absorbing boundary condition for wave equation modeling. J. Geophys. Eng. 15 (6), 2602—2613. https://doi.org/10.1088/1742-2140/aadd31.
- Liu, H., Zhang, H., 2019. Reducing computation cost by Lax-Wendroff methods with fourth-order temporal accuracy. Geophysics 84 (3), 1–64. https://doi.org/ 10.1190/geo2018-0196.1.
- Liu, D.J., Huang, J.P., Wang, Z.Y., 2020. Convolution-based multi-scale envelope inversion. Petrol. Sci. 17 (2), 352–362. https://doi.org/10.1007/s12182-019-00419-8
- Lysmer, J., Drake, L.A., 1972. A finite element method for seismology. Methods Comput. Phys. 11, 181–216. https://doi.org/10.1016/B978-0-12-460811-5.50009-X.
- Ma, X., Li, Y., Song, J., 2019. A stable auxiliary differential equation perfectly matched layer condition combined with low-dispersive symplectic methods for solving second-order elastic wave equations. Geophysics 84 (4), 1–57. https://doi.org/ 10.1190/geo2018-0572.1.
- Martin, R., Komatitsch, D., Gedney, S.D., et al., 2010. A high-order time and space formulation of the unsplit perfectly matched layer for the seismic wave equation using auxiliary differential equations(ADEPML). Comput. Model. Eng. Sci. 56 (1), 17–42. https://doi.org/10.3970/cmes.2010.056.017.
- Matzen, R., 2011. An efficient finite element time-domain formulation for the elastic second-order wave equation: a non-split complex frequency shifted convolutional PML. Int. J. Numer. Methods Eng. 88 (10), 951–973. https://doi.org/10.1002/nme.3205.
- Rabinovich, D., Givoli, D., Bécache, Eliane, 2010. Comparison of high-order absorbing boundary conditions and perfectly matched layers in the frequency domain. Int. J. Numer. Methods. Biomed. Eng. 26 (10), 1351–1369. https:// doi.org/10.1002/cnm.1394.
- Ren, Z.M., Liu, Y., 2014. Numerical modeling of the first order elastic equations with the hybrid absorbing boundary condition. Chin. J. Geophys. 57 (2), 595–606. https://doi.org/10.6038/cjg20140223.

Ren, Z., Liu, Y., Sen, M.K., 2017. Least-squares reverse time migration in elastic media. Geophys. J. Int. 208 (2), 1103–1125. https://doi.org/10.1093/gji/ggw443.

- Ren, Z., Bao, Q., Gu, B., 2021. Joint wave-equation traveltime inversion of diving/ direct and reflected waves for P- and S-wave velocity macromodel building. Geophysics 86 (4), R603—R621, https://doi.org/10.1190/geo2020-0762.1.
- Ren, Z., Bao, Q., Xu, S., 2022. Memory-efficient source wavefield reconstruction and its application to 3D reverse time migration. Geophysics 87 (1), S21–S34. https://doi.org/10.1190/geo2020-0580.1.
- Roden, J.A., Gedney, S.D., 2000. Convolution PML (CPML): an efficient FDTD implementation of the CFS-PML for arbitrary media. Microw. Opt. Technol. Lett. 27, 334–339. https://doi.org/10.1002/1098-2760.
- Roger, M.M., Marco, A., Jorge, L.M., et al., 2014. Frequency-domain acoustic-wave modeling with hybrid absorbing boundary conditions. Geophysics: J. Soc. Explor. Geophys. 79 (5), A39–A44. https://doi.org/10.1190/geo2014-0085.1.
- Song, P., Liu, Z., Zhang, X., et al., 2015. The fourth-order absorbing boundary condition with optimized coefficients for the simulation of the acoustic equation. J. Geophys. Eng. 12 (6), 996–1007. https://doi.org/10.1088/1742-2132/12/6/996.
- Takekawa, J., Mikada, H., 2016. An absorbing boundary condition for acoustic wave propagation using a mesh-free method. Geophysics 81 (4), T145—T154. https:// doi.org/10.1190/geo2015-0315.1.
- Virieux, J., 1984. SH-wave propagation in heterogeneous media: velocity-stress finite-difference method. Geophysics 49 (11), 1933—1942. https://doi.org/ 10.1071/EG984265a.
- Wang, E., Liu, Y., 2017. The hybrid absorbing boundary condition for one-step extrapolation and its application in wavefield decomposition-based reverse time migration. J. Geophys. Eng. 14 (4). https://doi.org/10.1088/1742-2140/ aa7308.
- Wang, Y., Zhou, H., Chen, H.M., et al., 2017. Adaptive stabilization for q-compensated reverse time migration. Geophysics 83 (1), S15–S32. https://doi.org/10.1190/ geo2017-0244.1.
- Wang, N., Zhou, H., Chen, H., et al., 2018. A constant fractional-order viscoelastic wave equation and its numerical simulation scheme. Geophysics 83 (1), 1–59. https://doi.org/10.1190/geo2016-0609.1.
- Wang, Z., Huang, J.P., Liu, D.J., et al., 2019a. 3D variable-grid full-waveform inversion on GPU. Petrol. Sci. 16 (5), 1001–1014. https://doi.org/10.1007/s12182-019-00368-2.
- Wang, E., Carcione, J.M., Ba, J., et al., 2019b. Nearly perfectly matched layer absorber for viscoelastic wave equations. Geophysics 84 (5), T335—T345. https://doi.org/ 10.1190/geo2018-0732.1.
- Wang, N., Zhu, T., Zhou, H., 2019c. Fractional Laplacians viscoacoustic wavefield modeling with k-space based time-stepping error compensating scheme. Geophysics 85 (1), 1–61. https://doi.org/10.1190/geo2019-0151.1.
- Wang, Y., Bai, M., Yang, Li, et al., 2021. An unsplit CFS-PML scheme for the second-Order wave equation with its application in fractional viscoacoustic simulation. IEEE Trans. Geosci. Rem. Sens. 60, 1–11. https://doi.org/10.1109/ TGRS.2021.3092714.
- Wang, N., Xing, G., Zhu, T., et al., 2022. Propagating seismic waves in VTI attenuating

- media using fractional viscoelastic wave equation. J. Geophys. Res. Solid Earth 127, e2021|B023280. https://doi.org/10.1029/2021|B023280.
- Xie, C., Song, P., Tan, J., et al., 2020. Cosine-type weighted hybrid absorbing boundary based on the second-order Higdon boundary condition and its GPU implementation. J. Geophys. Eng. 17 (2), 231–248. https://doi.org/10.1093/jge/gxz102.
- Xing, G., Zhu, T., 2019. Modeling frequency-independent Q viscoacoustic wave propagation in heterogeneous media. J. Geophys. Res. Solid Earth 124 (11), 11568–11584. https://doi.org/10.1029/2019JB017985.
- Xue, H., Liu, Y., Yang, Z.Q., 2018. Least-square reverse time migration of finite-difference acoustic-wave equation based on optimal time-space dispersion relation. Oil Geophys. Prospect. 53 (4), 745–753. https://doi.org/10.13810/j.cnki.issn.1000-7210.2018.04.011.
- Yao, G., da Silva, N.V., Wu, D., 2018. An effective absorbing layer for the boundary condition in acoustic seismic wave simulation. J. Geophys. Eng. 15 (2), 495–511. https://doi.org/10.1088/1742-2140/aaa4da.
- Yao, G., Wu, D., Wang, S.X., 2020. A review on reflection-waveform inversion. Petrol. Sci. 17 (1), 334–351. https://doi.org/10.1007/s12182-020-00431-3.
- Yuan, S., Wang, S., Sun, W., et al., 2014. Perfectly matched layer on curvilinear grid for the second-order seismic acoustic wave equation. Explor. Geophys. 45 (2), 94–104. https://doi.org/10.1071/EG13066.
- Zou, Q., Huang, J.P., Yong, P., et al., 2020. 3D elastic waveform modeling with an optimized equivalent staggered-grid finite-difference method. Petrol. Sci. 17 (4), 967–989. https://doi.org/10.1007/s12182-020-00477-3.
- Zhang, Y., Zhang, G., 2009. One-step extrapolation method for reverse time migration. Geophysics 74 (4), A29–A33. https://doi.org/10.1190/1.3123476.
- Zhang, W., Shen, Y., 2010. Unsplit complex frequency-shifted PML implementation using auxiliary differential equations for seismic wave modeling. Geophysics 75 (4), T141—T154. https://doi.org/10.1190/1.3463431.
- Zhang, W., Shi, Y., 2019. Imaging conditions for elastic reverse time migration. Geophysics 84 (2), S95–S111. https://doi.org/10.1190/GEO2018-0197.1.
- Zhang, W., Gao, J., Gao, Z., et al., 2020. 2D and 3D amplitude-preserving elastic reverse time migration based on the vector-decomposed P- and S-wave records. Geophys. Prospect. 68 (9), 2712–2737. https://doi.org/10.1111/1365-2478.13023.
- Zhang, W., Gao, J., Yang, T., et al., 2021. Least-squares reverse time migration using convolutional neural network. Geophysics 86 (6), R959—R971. https://doi.org/ 10.1190/geo2021-0006.1.
- Zhao, Y., Liu, Y., Ren, Z.M., 2014. Viscoacoustic prestack reverse time migration based on the optimal time—space domain high-order finite-difference method. Appl. Geophys. 11 (1), 50–62. https://doi.org/10.1007/s11770-014-0414-8.
- Zhu, T., Harris, J.M., 2014. Modeling acoustic wave propagation in heterogeneous attenuating media using decoupled fractional Laplacians. Geophysics 79 (3), T105–T116. https://doi.org/10.1190/geo2013-0245.1.
- Zhuang, M., Zhan, Q., Zhou, J., et al., 2020. A simple implementation of pml for second-order elastic wave equations. Comput. Phys. Commun. 246 (1), 106867. https://doi.org/10.1016/j.cpc.2019.106867.